

Visualizing Three-dimensional Flow with Simulated Streamlines and Three-dimensional Phase-Contrast MR Imaging¹

Sandy Napel, PhD • Donald H. Lee, MD • Richard Frayne, BSc • Brian K. Rutt, PhD

Three-dimensional (3D) velocity maps acquired with 3D phase-contrast magnetic resonance (MR) imaging contain information regarding complex motions that occur during imaging. A technique called *simulated streamlines*, which facilitates the display and comprehension of these velocity data, is presented. Single or multiple seed points may be identified within blood vessels of interest and tracked through the velocity field. The resulting trajectories are combined with a 3D MR angiogram and displayed with 3D volume visualization software. Mathematical analysis highlights potential applications and pitfalls of the technique, which was implemented both in phantoms and in vivo with excellent results. For example, single streamlines reveal helical flow patterns in aneurysms, and multiple streamlines seeded in the common carotid artery reveal branch filling-time relationships and slow filling of the carotid bulb. The technique is helpful in understanding these complex flow patterns.

Index terms: Image display • Image processing • Magnetic resonance (MR), experimental • Model, mathematical • Phantoms • Physics • Reconstruction algorithms • Three-dimensional studies • Vascular studies

JMRI 1992; 2:143-153

Abbreviations: PC = phase contrast, 3D = three-dimensional, 2D = two-dimensional.

¹ From the Department of Radiology, S-047, Stanford University School of Medicine, 300 Pasteur Dr, Stanford, CA 94305-5105 (S.N.); the Departments of Diagnostic Radiology and Nuclear Medicine (D.H.L., B.K.R.) and Medical Biophysics (R.F., B.K.R.), University of Western Ontario, London, Ont, Canada; and the Tom Lawson Family Imaging Research Laboratories, John P. Robarts Research Institute, London, Ont, Canada (R.F., B.K.R.). Received October 11, 1991; revision requested November 19; revision received December 20; accepted December 23. Supported by the Natural Sciences and Engineering Research Council of Canada, the Medical Research Council of Canada, and GE Medical Systems. **Address reprint requests to S.N.**

© SMRI, 1992

PHASE-CONTRAST (PC) magnetic resonance (MR) imaging can produce quantitative maps of three-dimensional (3D) velocity vectors in an acquired 3D slab (1-9). The results are generally organized into three sets of reconstructed sections, one set for each of the x, y, and z components of the velocity vectors. Each section consists of 256×256 16-bit pixels, and there are as many sections as required to cover the volume of interest. For example, if each section is 0.5 mm thick, 40 sections are required to cover a 20-mm slab through the brain. In this case, 120 images (15 Mbytes) that contain the desired velocity information will be reconstructed. The present study addresses two problems that arise when attempting to review this type of data: It can be quite time-consuming to review such a large number of images, and, even if that were not a problem, the organization of the data into the three components of velocity makes visualization of flow difficult.

To illustrate these points, consider Figure 1. It shows three components of velocity vectors imaged in a single 0.7-mm-thick coronal plane of a 3D PC MR study of the brain obtained with a balanced four-point method (10) on a 1.5-T Signa Advantage imager (GE Medical Systems, Milwaukee). In each of the three images (a-c), photographed at identical level and window settings, the gray scale maps magnitude and direction of velocity along a specified axis: Figure 1a maps velocity along the anteroposterior axis, Figure 1b from right to left, and Figure 1c along the superoinferior axis. Zero velocity is represented as a midrange shade of gray; anteroposterior, right-to-left, and superoinferior flows are encoded in lighter shades, and flow from the opposite directions (posteroanterior, left to right, and inferosuperior) is encoded in darker shades on the respective images. The anatomic location is through a large intracranial aneurysm, within which the three arrowheads point to corresponding pixels in each of the three images. By noting the direction of flow in each of the three component images at each of the arrowheads, one can conclude that within the aneurysm in this plane, flow is in a counterclockwise direction, and that blood flow is anteroposterior in the inferior portion and poster-

Figure 1. Representative PC MR images of a single 0.7-mm-thick coronal plane through the center of a giant basilar tip aneurysm. (a–c) Three components of velocity, each with zero velocity encoded as a middle shade of gray: (a) anteroposterior (A–P) component, with lighter shades indicating anteroposterior flow and darker shades posteroanterior flow; (b) right-left (R–L) component, with lighter shades indicating right-to-left flow and darker shades left-to-right flow; (c) superoinferior (S–I) component, with lighter shades indicating superoinferior flow and darker shades inferosuperior flow. Three arrowheads point to corresponding pixels in the three component images. (d) “Speed” image is computed as the magnitude of the velocity vector at each pixel, zero speed being encoded as black and higher speeds as increasingly brighter shades.



oanterior in the superior portion. Further inspection of relative intensities on each of the three images shows that anteroposterior and posteroanterior speeds are less than those in the coronal plane. Although it may be possible to learn to distinguish this particular flow pattern from the three component images, generalized flow patterns will be more difficult to discern. Furthermore, appreciation of the true 3D nature of complex flow patterns requires inspection of all sections and mental reconstruction of the 3D flow patterns. In summary, evaluating complex flow patterns from the three component images of each reconstructed plane may not be practical, if even possible.

We propose an alternate means of displaying flow patterns, called *simulated streamlines* (11), that reduces the 3D velocity information from a 3D PC MR imaging study into a set of 3D streamlines that can be displayed with standard 3D display software. Instead of attempting to assimilate a picture of flow patterns by looking at hundreds of images, the observer can pick one or many “seed particles” within vessels of interest, track their calculated motion through the acquired velocity field, and display the resulting streamlines in rotating cine loops or stereo pairs. In addition to aiding the visualization of complex flow patterns, time relationships (eg, vessel filling/emp-

tying patterns) can be easily observed by displaying the evolution of these simulated streamlines as a function of time. Previously, these time relationships were observable in vivo only with contrast agent-enhanced x-ray angiography.

• METHODS

Theory

Generation of simulated streamlines is a four-step process:

1. An estimate of the 3D velocity field within a volume of anatomy is generated.
2. Single or multiple seed particles within vascular structures of interest are selected.
3. Three-dimensional seed particle trajectories are computed (simulated) by using the velocity estimate obtained in step 1.
4. The resulting trajectories (ie, the simulated streamlines) are displayed.

Step 1 is accomplished with a 3D PC MR technique that uses four acquisitions to compute three orthogonal components of velocity in every voxel in the acquired slab (10). (Theoretically, a contiguous stack of two-dimensional [2D] PC images could be used, but a

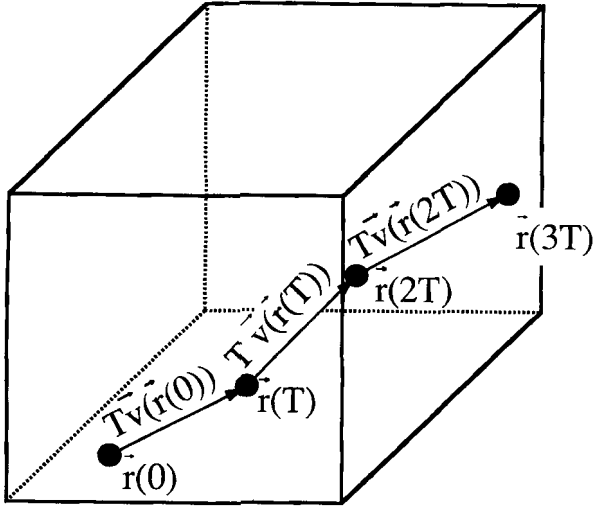


Figure 2. Graphical representation of the simulated-streamline algorithm. Given a simulation time step T , a seed particle at 3D position $\mathbf{r}(T)$ with initial velocity $\mathbf{v}(\mathbf{r}(T))$ will follow the illustrated trajectory through the velocity field.

3D acquisition is preferred because of the superior through-plane resolution available.) We assume that spins within each voxel move identically, that velocities are constant during the entire acquisition, and that any higher-order motions are negligible. If we denote a location within the slab by

$$\mathbf{r} = (x, y, z), \quad (1)$$

the acquired velocity field may be written as

$$\mathbf{v}(\mathbf{r}) = [v_x(\mathbf{r}), v_y(\mathbf{r}), v_z(\mathbf{r})], \quad (2)$$

where $v_x(\mathbf{r})$, $v_y(\mathbf{r})$, and $v_z(\mathbf{r})$ are the three measured components of velocity.

Step 2 requires an anatomic map of blood vessels from which to choose seed particles for the simulation. We compute the “speed volume,”

$$v(\mathbf{r}) = |\mathbf{v}(\mathbf{r})| = \sqrt{v_x^2(\mathbf{r}) + v_y^2(\mathbf{r}) + v_z^2(\mathbf{r})}, \quad (3)$$

for this purpose because it enables depiction of bright vessels contrasting with darker static structures.

The simulation (step 3) tracks the position

$$\mathbf{r}(t) = [x(t), y(t), z(t)] \quad (4)$$

of each seed particle as a function of simulation time t as the particle moves through the acquired velocity field. Starting at $t = 0$, the position of this particle can be expanded in a Taylor series:

$$\mathbf{r}(t) = \mathbf{r}(0) + \mathbf{v}(\mathbf{r}(0))t + \frac{1}{2}\mathbf{a}(\mathbf{r}(0))t^2 + \dots, \quad (5)$$

where $\mathbf{r}(0)$ is the initial location of the particle and \mathbf{a} is the acceleration. The initial velocity $\mathbf{v}(\mathbf{r}(0))$ can be obtained from the acquired velocity field. For the present, we assume that the acceleration, and higher-order motion terms are negligible. If we define a sampling interval T , we compute the location of the particle at time $t = T$ to be

$$\mathbf{r}(T) = \mathbf{r}(0) + \mathbf{v}(\mathbf{r}(0))T. \quad (6)$$

The velocity at this new location, $\mathbf{r}(T)$, can, as before, be obtained from the velocity field and used to compute the next location at time $t = 2T$. In general, then, we can write

$$\begin{aligned} \mathbf{r}(kT) &= \mathbf{r}(0) + \mathbf{v}(\mathbf{r}(0))T + \mathbf{v}(\mathbf{r}(T))T + \mathbf{v}(\mathbf{r}(2T))T \dots \\ &= \mathbf{r}(0) + T \sum_{j=0}^{k-1} \mathbf{v}(\mathbf{r}(jT)), \end{aligned} \quad (7)$$

which can be written in recursive form as

$$\mathbf{r}(kT) = \mathbf{r}[(k-1)T] + \mathbf{v}[\mathbf{r}[(k-1)T]]T. \quad (8)$$

Equation (8) is the basic equation of motion used in the simulation. Figure 2 illustrates the algorithm as a simple sum of 3D vectors. At time kT , the velocity of the particle is obtained from the velocity field, scaled by T , and added to the current position to compute its next position.

Two practical points should be mentioned at this time:

1. T must be chosen to ensure that simulated streamlines do not skip any voxels in the measured velocity field. There are two ways to do this: (a) A single T can be chosen on the basis of the maximum speed expected, v_{\max} , and the minimum voxel dimension d , such that

$$T < \frac{d}{2v_{\max}}, \quad (9)$$

or (b) T can be chosen at each iteration step k as a function of local velocity. Though we have used both techniques, the first computes simulated streamlines at constant time intervals and behavior is easier to analyze than with the second. Thus, the remainder of this report assumes a single sampling interval T that satisfies Equation (9).

2. Particle trajectories will not, in general, pass through the center of voxels in the measured velocity field. Therefore, interpolation must be used to obtain the local velocities. Though elaborate interpolation schemes may be used, prohibitive computation time penalties may be incurred for algorithms more complex than first-order (ie, trilinear) interpolation. Implications of this interpolation step will be discussed below.

Finally, step 4 combines each 3D streamline trajectory $\mathbf{r}(kT)$ with the speed volume $v(\mathbf{r})$, so that the simulated streamlines appear within a depiction of vascular anatomy. This may be done in a number of ways. For example, if we encode $v(\mathbf{r})$ in shades of gray, color can be used to distinguish individual streamlines, or color can be used to encode local speed along a trajectory. In either case, the result is a 3D volume that may be visualized with a 3D volume visualization package, either by transparent reprojection (eg, density sum, maximum-intensity projection) or shaded surface display, from one or many angles. Cine loops of rotating volumes or stereo pairs may be used to convey depth.

Effects of Noise

Effects of random noise on the simulated streamlines are difficult to describe. Some general statements that may be made are the following:

1. Effects of random noise are functions of the noise statistics and the underlying velocity field.
2. Random noise may bias the expected streamline position away from the streamline position that might have been computed under zero-noise conditions.
3. Random noise may result in increased uncertainty in the component of the streamline position along the flow direction relative to the components in directions orthogonal to flow.
4. Effects of random noise accumulate during the simulation; that is, uncertainty in the location of the streamline increases with simulation time t .

These statements beg for velocity estimates with the best signal-to-noise ratio possible. However, because a signal-to-noise ratio of infinity is impractical, it is important to understand the effects of noise on the simulated streamline images. Suppose

$$\mathbf{v}(\mathbf{r}) = \bar{\mathbf{v}}(\mathbf{r}) + \mathbf{n}_v(\mathbf{r}), \quad (10)$$

where $\bar{\mathbf{v}}(\mathbf{r})$ is the true velocity and $\mathbf{n}_v(\mathbf{r})$ is a sample of the noise. We assume that the noise is zero-mean, or

$$\begin{aligned} \mathbf{E}[\mathbf{n}(\mathbf{r}(jT))] &= (E[n_{v_x}(\mathbf{r}(jT))], E[n_{v_y}(\mathbf{r}(jT))], E[n_{v_z}(\mathbf{r}(jT))]) \\ &= (0, 0, 0) = \mathbf{0}, \end{aligned} \quad (11)$$

and the noise in the x , y , and z directions is uncorrelated with variance, or

$$\overrightarrow{\text{Var}}[\mathbf{n}(\mathbf{r}(jT))] = \overrightarrow{\sigma_{\mathbf{n}_v}^2} = (\sigma_{n_{v_x}}^2, \sigma_{n_{v_y}}^2, \sigma_{n_{v_z}}^2). \quad (12)$$

The variance depends both on signal magnitude and on the change in the first moment ΔM_1 of the gradient waveform used to encode velocity (10). Though we can assume identical ΔM_1 on each axis, we cannot, in general, assume spatially constant signal magnitude and, therefore, spatially invariant noise. For simplicity, however, we will assume a spatially constant variance defined as

$$\overrightarrow{\sigma_{\mathbf{n}_v}^2} = \overrightarrow{\sigma^2} = (\sigma^2, \sigma^2, \sigma^2), \quad (13)$$

where σ^2 can be any value we choose (possibly representative of the worst-case variance), to study simulated-streamline position errors.

If we substitute Equation (10) into Equation (7), the streamline position at the k th iteration is

$$\mathbf{r}(kT) = \mathbf{r}(0) + T \sum_{j=0}^{k-1} \bar{\mathbf{v}}(\mathbf{r}(jT)) + T \sum_{j=0}^{k-1} \mathbf{n}_v(\mathbf{r}(jT)). \quad (14)$$

Note that, in general, both the second and third terms of Equation (14) contribute to the error, because for $j \neq 0$, $\bar{\mathbf{v}}(\mathbf{r}(jT))$ is a function of an erroneous position. Thus, the error introduced by noise is not only a function of the noise statistics but is also a function of the true velocity field. In some cases, this complication may result in substantial errors in computed streamline position. For example, near bifurcations, noise samples may determine which branch is taken by the streamline. Thus, even with the simplifying assumptions of Equations (11)–(13), it is quite difficult to generalize quantitative effects of noise. The following

examples provide some insight by illustrating these effects in specific cases. Note that the examples use the additional simplifying assumption that first-order (ie, “nearest-neighbor”) interpolation is used to determine velocities along streamline trajectories.

Example 1: $\bar{\mathbf{v}}(\mathbf{r}) = \mathbf{0}$ for all \mathbf{r} .

This is the trivial no-flow case. Equation (14) becomes

$$\mathbf{r}(kT) = \mathbf{r}(0) + T \sum_{j=0}^{k-1} \mathbf{n}_v(\mathbf{r}(jT)), \quad (15)$$

with the expected value

$$\mathbf{E}[\mathbf{r}(kT)] = \mathbf{r}(0) \quad (16)$$

and variance

$$\overrightarrow{\text{Var}}[\mathbf{r}(kT)] = T^2 \overrightarrow{\text{Var}} \left\{ \sum_{j=0}^{k-1} \mathbf{n}_v(\mathbf{r}(jT)) \right\}. \quad (17)$$

If $\mathbf{r}(jT)$ is in the same voxel for all j , the variance is simply

$$\overrightarrow{\text{Var}}[\mathbf{r}(kT)] = (kT)^2 \overrightarrow{\sigma^2}. \quad (18)$$

However, suppose that during kT seconds the simulated streamline passes through M voxels and spends $k_i T$ seconds in each voxel $i \in [1, M]$. If we assume independent noise contributions from each voxel and spatially constant noise (Equation [13]), the variance will be the sum of the variance contributed by each voxel, or

$$\overrightarrow{\text{Var}}[\mathbf{r}(kT)] = \sum_{i=1}^M (k_i T)^2 \overrightarrow{\sigma^2}. \quad (19)$$

The quantity $k_i T$ can be thought of as the dwell time of the simulated streamline in the i th voxel. Thus, Equations (16) and (19), combined, tell us that, in the mean, the seed particle will not move from its initial position and the variance grows with the sum of the squares of the dwell time in each voxel. Unfortunately, the dwell time is difficult to determine, even in this trivial case of zero flow. However, Equation (19) does give us a formula by which, given the velocity variance in each voxel, one can compute the position variance at a given iteration retrospectively.

Example 2:

$$\bar{\mathbf{v}}(\mathbf{r}) = v_{\max} \left[1 - \left(\frac{x^2 + z^2}{\rho^2} \right) \right] \hat{\mathbf{y}} \text{ when } \sqrt{x^2 + z^2} \leq \rho,$$

$$\bar{\mathbf{v}}(\mathbf{r}) = \mathbf{0} \text{ when } \sqrt{x^2 + z^2} > \rho.$$

With ρ the radius of a cylindric vessel and $\hat{\mathbf{y}}$ a unit vector in the direction of flow, this is the case of a 2D parabolic velocity profile. To avoid the difficulties caused by slow flow (illustrated in the previous example), we will assume that the velocity noise is small enough that during the course of the simulation the trajectory has negligible probability of crossing the vessel wall. Thus, we can ignore the case $\sqrt{x^2 + z^2} > \rho$, and Equation (14) becomes

$$\mathbf{r}(kT) = \mathbf{r}(0) + Tv_{\max} \hat{\mathbf{y}} \sum_{j=0}^{k-1} \left[1 - \frac{x^2(jT) + z^2(jT)}{\rho^2} \right] + T \sum_{j=0}^{k-1} \mathbf{n}_y[\mathbf{r}(jT)]. \quad (20)$$

The x and z components of Equation (20) are identical to those of Equation (15) (zero flow case). Thus,

$$E[x(kT)] = x(0), \quad (21a)$$

$$E[z(kT)] = z(0), \quad (21b)$$

and

$$\text{Var}[x(kT)] = \text{Var}[z(kT)] = \sum_{i=1}^M (k_i T)^2 \sigma^2. \quad (21c)$$

However, in the y direction,

$$E[y(kT)] = y(0) + Tv_{\max} \sum_{j=0}^{k-1} \left[1 - \frac{E[x^2(jT)] + E[z^2(jT)]}{\rho^2} \right] + T \sum_{j=0}^{k-1} E[n_y[\mathbf{r}(jT)]]. \quad (22)$$

The third term, as in the zero flow case, is zero. The expected values in the second term may be obtained from the identity $\text{Var}(x) = E(x^2) - E^2(x)$, resulting in

$$E[y(kT)] = y(0) + Tv_{\max} \sum_{j=0}^{k-1} \left\{ 1 - \frac{x^2(0) + z^2(0) + \text{Var}[x(jT)] + \text{Var}[z(jT)]}{\rho^2} \right\}. \quad (23)$$

Substituting Equation (21c) into Equation (23) results in

$$E[y(kT)] = y(0) + kTv_{\max} \left[1 - \frac{x^2(0) + z^2(0)}{\rho^2} \right] - \frac{2T^3 v_{\max} \sigma^2}{\rho^2} \sum_{j=0}^{k-1} \sum_{i=1}^M j_i^2. \quad (24)$$

Equation (24) expresses the expected value as the initial position plus the sum of two terms. The first of these is independent of noise and shows, for example, that when the variance is zero, the seed particle moves in the direction of flow, as expected. In general, however, the expected value of the y component of the trajectory is reduced by the second of these terms, which is proportional to the noise variance. To see this, consider a seed particle at an arbitrary position in the vessel. Noise in the x and z directions will tend to move the initial trajectory away from its initial x and z position and thus to a region where the underlying velocity is not the same as at the initial position. Because of the parabolic flow profile, an error of a given magnitude in the direction of the vessel wall causes a bigger change in underlying velocity than the same error toward the center of the vessel. In this way, through Equation (24), noise in the velocity measurements perpendicular to the flow direction biases

the expected value of the simulated-streamline position toward zero.

The variance in the y component may be obtained from the y component of Equation (20):

$$\text{Var}[y(kT)] = \text{Var} \left\{ y(0) + Tv_{\max} \sum_{j=0}^{k-1} \left[1 - \frac{x^2(jT) + z^2(jT)}{\rho^2} \right] + T \sum_{j=0}^{k-1} n_y[\mathbf{r}(jT)] \right\}. \quad (25)$$

If we assume independence of the three terms, Equation (25) becomes

$$\text{Var}[y(kT)] = T^2 v_{\max}^2 \cdot \text{Var} \left\{ \sum_{j=0}^{k-1} \left[1 - \frac{x^2(jT) + z^2(jT)}{\rho^2} \right] \right\} + T^2 \text{Var} \left\{ \sum_{j=0}^{k-1} n_y[\mathbf{r}(jT)] \right\}. \quad (26)$$

The second term is simply the y component of Equation (19), the zero-velocity case, which is identical to the variance in the x and z directions (Eq [21c]). Because the first sum in Equation (26) is nonnegative, one observes that the variance in the y component is greater than in the other two directions. This can be understood by observing that noise in the x and z directions causes the particle to move to regions where the true speed in the y direction is faster or slower than at its initial position. It is also clear from Equation (26), that this additional variance grows with k. Thus, we can draw the qualitative conclusion that the variance in the y component "spreads out" in the y direction compared with the x and z directions.

Ignoring Higher-Order Motions in Simulated-Streamline Computation

Higher-order motions can arise because of time-varying magnitude and/or direction of lower-order motions. In particular, acceleration of particles along trajectories will, in general, not be zero, even in the case of constant flow. For example, a streamline that moves around a bend in a vessel at constant speed is accelerating because its direction is changing. However, Equation (8) ignores the higher-order motion terms of Equation (5) and, thus, may result in error. In general, these effects are small, as shown by the following examples.

Example 3: Effects of ignoring acceleration in curved trajectories.

Figure 3 shows a particle traveling along a curved path. Suppose its position at $t = 0$ is $\mathbf{r}(0)$ (labeled A) and the path at $\mathbf{r}(0)$ has a local radius of curvature $|\mathbf{r}(0)|$. If we accurately measure its velocity $\mathbf{v}[\mathbf{r}(0)]$ and use it in Equation (6) to compute its position a short time T later, we move along the vector $T\mathbf{v}[\mathbf{r}(0)]$ to the point labeled B. If we assume that only the first three terms in the Taylor series expansion of Equation (5) are significant (ie, the trajectory can be adequately approximated by a circle), in the limit of small T , the error incurred by ignoring the acceleration term is

$$\epsilon(T) = -\frac{T^2}{2} \mathbf{a}[\mathbf{r}(0)]. \quad (27)$$

The direction of this error instantaneously points back to the center of the radius of curvature. Thus, ignoring the acceleration term always underestimates the bend radius. The magnitude of this error is

$$|\epsilon(T)| = \frac{T^2}{2} \frac{|\mathbf{v}[\mathbf{r}(0)]|^2}{|\mathbf{r}(0)|}. \quad (28)$$

If we use the constraint on the sampling interval T given in Equation (9), the magnitude of the error can be bounded by

$$|\epsilon(T)| < \frac{d^2}{8v_{\max}^2} \frac{|\mathbf{v}[\mathbf{r}(0)]|^2}{|\mathbf{r}(0)|}. \quad (29)$$

The largest error, therefore, will occur when the local speed is equal to the maximum speed expected. Thus, Equation (29) becomes

$$|\epsilon(T)| < \frac{d}{8|\mathbf{r}(0)|} d. \quad (30)$$

The largest error will occur at the smallest possible radius of curvature. However, the smallest possible radius of curvature through which we can track particles is limited by our image resolution to d . In this case the error becomes one-eighth of the minimum voxel dimension (typically, $d < 1$ mm). A more likely minimum radius of curvature would be three to 10 times d , bounding the error in a single iteration to less than 1/24 to 1/800 mm. Thus, we conclude that the error is small and, for most practical purposes, can be ignored. However, as was the case for additive noise, this error is cumulative and its direction is such that simulated streamlines will tend to move to the outer edges of bending vessels, where measured speeds will decrease, as will signal magnitude. It may be necessary, therefore, to beware of this effect when simulating streamlines through lengthy vessel curves at high speeds.

Example 4: Maximum linear deceleration.

Suppose a particle moving with speed v_{\max} comes to rest in one sample period T . The magnitude of the error term in Equation (27) is

$$|\epsilon(T)| = \frac{T^2}{2} \frac{|-v_{\max}|}{T} = T \frac{v_{\max}}{2}. \quad (31)$$

By again using the constraint of Equation (9),

$$|\epsilon(T)| < \frac{d}{4}. \quad (32)$$

Therefore, for the typical case in which $d < 1$ mm, the magnitude of the error is bounded by 0.25 mm. The direction of the error is opposite to the direction of flow; thus, ignoring the acceleration term in this case overestimates the distance traveled during the sampling interval. Again, we note that the error in this extreme case is small and, therefore, in most cases can be ignored; however, it is cumulative and, because ignoring it overestimates distance traveled, particle positions may tend to be computed beyond vessel boundaries.

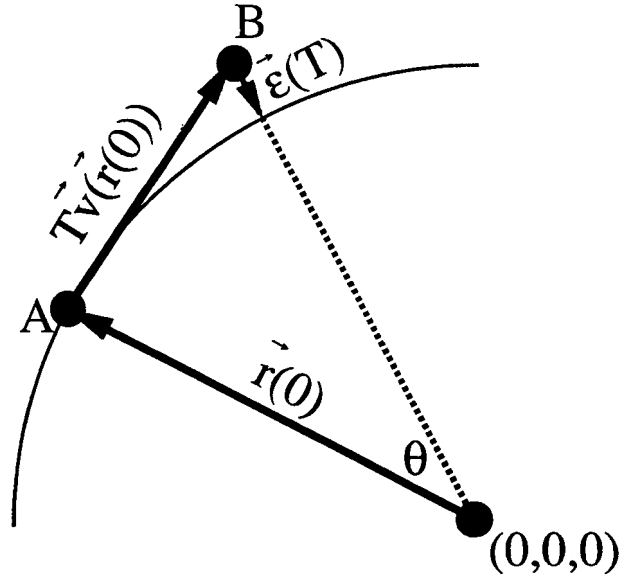


Figure 3. Illustration of error incurred by ignoring acceleration term (Eq [5]) in simulated-streamline computation. For small θ , as a particle travels with constant speed from point A around a circular path, the error points toward center of radius of curvature. The magnitude of the error is small when bounded by practical constraints (see text).

Velocity Measurement Errors Due to Higher-Order Motions

The acceleration and higher-order motions experienced by the spins in the fluid cause errors in the velocity estimates obtained with PC MR imaging. Recent work has shown that a bipolar velocity-encoding sequence accurately measures the component of velocity along an axis at a particular time point (if jerk and the other higher-order odd terms are ignored) (12,13). The time at which the accurate velocity measurement is made need not be the same as the time that the position measurement is made. The implications of this are best described with Figure 4, which represents the trajectory of a spin $\mathbf{r}(\tau)$. If, for now, we assume that the three components of position are acquired simultaneously at time $\tau = TE$, and that the three components of velocity are acquired simultaneously at time $\tau = TE - \delta\tau$, the velocity estimate made with PC MR imaging is equal to $\mathbf{v}[\mathbf{r}(TE - \delta\tau)]$ instead of $\mathbf{v}[\mathbf{r}(TE)]$. The error in the PC MR velocity estimate $\delta\mathbf{v}$ is the difference in velocity between the two measurement times:

$$\delta\mathbf{v} = \mathbf{v}[\mathbf{r}(TE)] - \mathbf{v}[\mathbf{r}(TE - \delta\tau)]. \quad (33)$$

If the spatial trajectory does not pass through an inflection point during $\delta\tau$, then the error tends to resist any change in direction, as can be seen in Figure 4. Consider, for example, a particle traveling in a circular trajectory with a radius of 1 cm at a speed of 20 cm/sec (representative of flow patterns found in aneurysms or tight curves). Suppose we acquire velocity estimates with a PC MR imaging technique with a $\delta\tau$ of 5 msec. In this case, Equation (33) computes the error to be 2 cm/sec, with a direction that will cause a

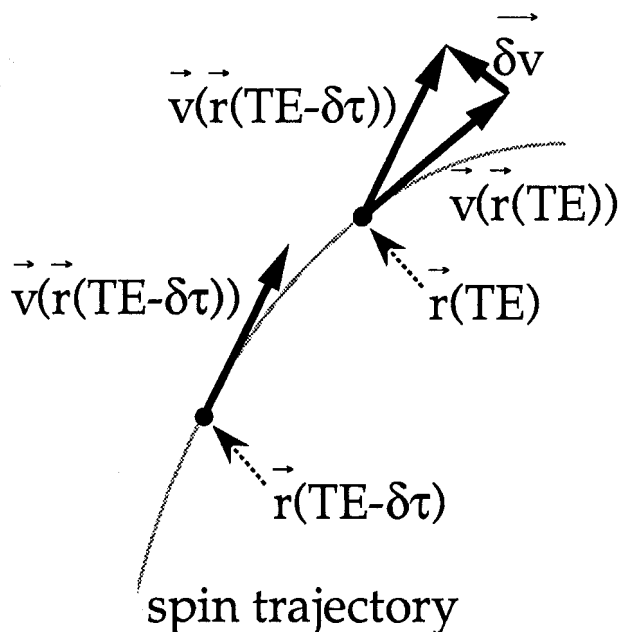


Figure 4. Illustration of velocity measurement error caused by encoding velocity and position at different times. Accurate velocity is measured at time $TE - \delta\tau$, but position is not encoded until time TE . In the meantime, the spin has moved and its velocity may have changed.

simulated streamline to gradually spiral away from the circular trajectory. Though in this case of fairly high acceleration the error is small (10%), it may partially explain the increased number of “leakers” (simulated streamlines that pass through vessel walls) found in regions of high acceleration. Also note that the simplifying assumption of simultaneous acquisition of three components of position (or velocity) is not satisfied by practical pulse sequences. As a result, the acquired velocity field used as data for the simulated-streamline algorithm contains errors that are due to any change in velocity experienced by the spins during the measurement time. This error may explain the increased “leakage” when particles are followed around tight curves, where large accelerations are present.

• RESULTS

We simulated streamlines with velocity data obtained in phantoms, healthy volunteers, and patients. We describe the data and results and illustrate several applications of the technique. All phantoms were supplied with a constant flow by using a computer-controlled flow simulator (14,15).

Phantom Studies

Figure 5 is an oblique reprojection along the anteroposterior axis of results obtained from a semicircular tube phantom with an inner diameter of 6.36 mm and a radius of curvature of 50 mm. Three-dimensional PC MR imaging data were acquired with the following parameters: 12.8-cm field of view, 28 0.4-mm-thick sections, and a constant flow rate of 3.1 mL/sec. The simulated streamlines are extremely smooth and

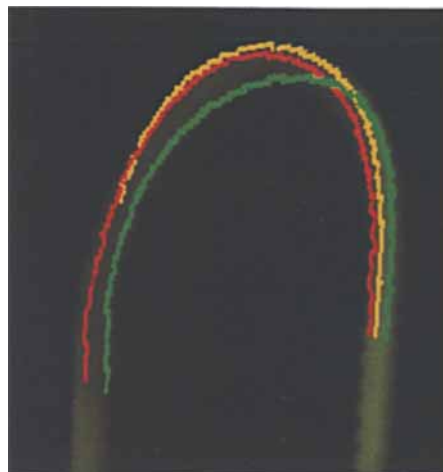
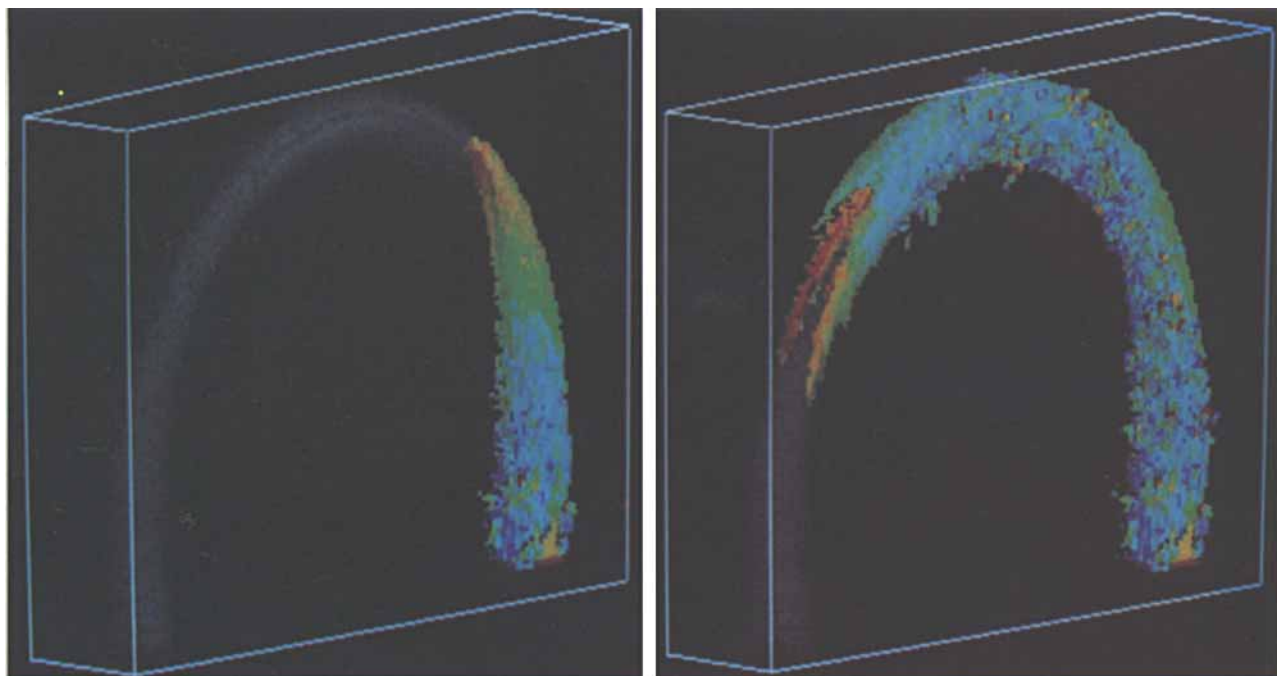


Figure 5. Oblique reprojection of three simulated streamlines through a semicircular tube phantom with constant flow at 3.1 mL/sec. The speed volume is represented in shades of gray, and three colors are used to distinguish the three streamlines. The seed particles originated along a line through the center of the inflow tube normal to the plane of the bend and were separated by 0.8 mm (red-yellow) and 1.6 mm (yellow-green).

curve gently around the tube from inflow to outflow. Though difficult to see in a single 2D rendition (ie, without the benefit of cine rotation or stereo cues), these traces show spiraling flow that occurs after entry of the streamline into the semicircular region.

Figure 6a shows another way of visualizing the same data as above; however, in this case, 968 seed particles (eight particles per voxel) covering a “block” intersecting the inflow tube were tracked. Also, the color of each streamline at any point indicates local speed according to a “pseudo-Doppler” scale (blue = slow, red = fast). Each simulated streamline was computed, and the resulting set of streamlines was reprojected with a shaded-surface display technique. Thus, the Figure depicts the outer surface of the streamlines for 50 msec of simulation time. Laminar flow is easily visualized by noting the slow-moving outer shell and the progressively faster-moving particles in more central portions of the inflow. Figure 6b shows the results of the same simulation after 150 msec. Here, one can see a distinctive flow separation in the semicircular region reminiscent of previously published data obtained with other techniques (16). Also note that comparing Figure 6a and 6b (or, better yet, observing a sequence of these images in a cine loop) gives a strong impression of filling patterns, reminiscent of that of an actual bolus of contrast material.

Figure 7 is sagittal reprojection showing three simulated streamlines through an anatomically accurate carotid bifurcation phantom (17). Acquisition parameters were an 8-cm field of view, 28 0.7-mm-thick sections, and a flow rate 7.1 mL/sec, with a ratio of flow rates of .7/.3 for the external/internal branches. The



a.

b.

Figure 6. Shaded surface display of the trajectories of a “block” of 968 seed particles in the semicircular tube phantom after 50 msec of simulation time (a) and after 150 msec of simulation time (b). Color indicates speed (blue = slow, red = fast) on the surface of the “cloud” of streamlines as it travels through the tube. Sequences of these images viewed in a cine loop reveal complex flow patterns and time relationships previously available only through use of contrast material in x-ray angiography.

two streamlines on the right were placed at the center (in the right-left direction) of the common carotid artery, and the third was placed 1.4 mm off center. Pseudo-Doppler color coding (brightest red = 40 cm/sec ↔ darkest blue = 0 cm/sec) was used to show speed on the static image. Note that the streamline at the farthest right curves slowly through the carotid bulb, which is consistent with well-known phenomena and observable with other techniques (18,19).

In Vivo Studies

Figure 8 shows results of data obtained from the right carotid artery in a healthy volunteer. Acquisition parameters were an 18-cm field of view and 28 0.7-mm-thick sections. A block of 75 seed particles (one particle per voxel) was placed in the common carotid artery, and the simulation proceeded for 225 msec. The image is a sagittal maximum-intensity projection (20) through the speed volume (gray scale) combined with a pseudo-Doppler-encoded set of streamlines. In this mode, the color scale represents the highest speed along the reprojected ray (with brightest red = 40 cm/sec). Note the slowly filling carotid bulb and the successful propagation of streamlines into the internal and external branches, as well as the facial artery.

Figure 9a and 9b shows results of a single simulated streamline within the giant basilar tip aneurysm shown in Figure 1. Acquisition parameters were a 20-cm field of view and 28 1-mm-thick sections. The seed particle was placed in a region of the aneurysm

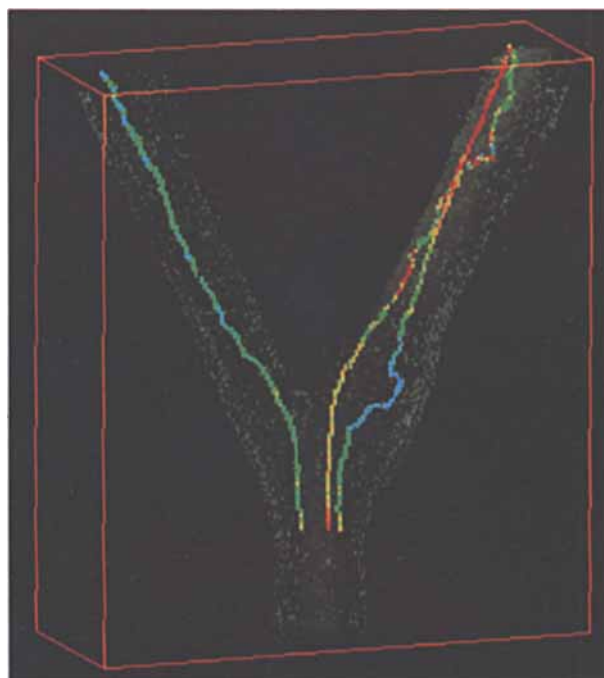


Figure 7. Sagittal reprojection of three simulated streamlines through a carotid bifurcation phantom. Color indicates local speed along streamline (blue = 0 cm/sec, red = 40 cm/sec). The streamline that moves slowly through the carotid bulb was initially placed 1.4 mm off center in the right-left direction.

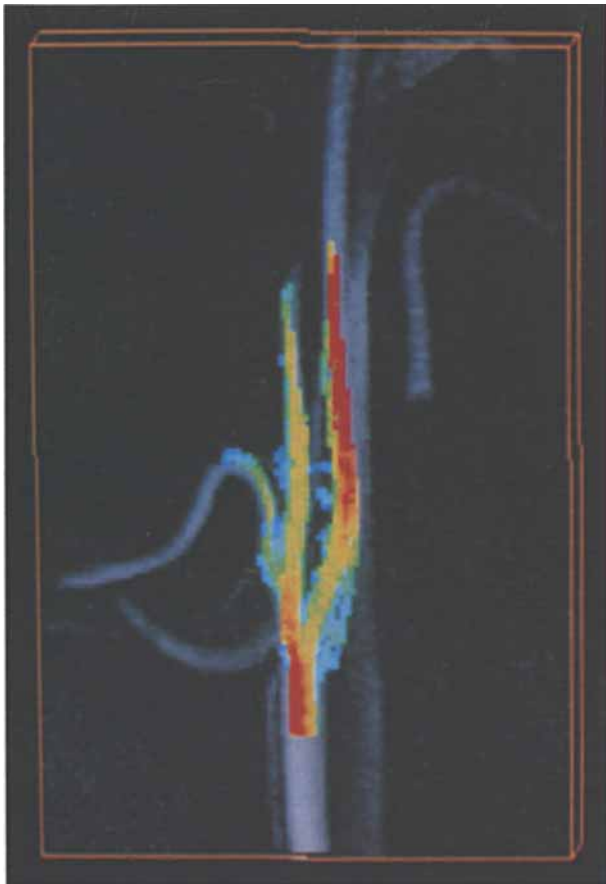


Figure 8. Color-coded (blue = 0 cm/sec, red = 40 cm/sec) maximum-intensity reprojec-tion of a block of 75 seed particles placed in the common carotid artery of a healthy volunteer.

farthest from the originating artery, and pseudo-Doppler encoding was used (brightest red = 25 cm/sec \leftrightarrow darkest blue = 0 cm/sec). Note the helical pattern showing blood swirling back to the inflow, with the streamline finally "leaking" through the aneurysm wall. We suspect that the leakage may be caused by greater noise in the vicinity of the wall, which is caused by smaller signal magnitude (10) due to saturation of slowly moving blood. These two static images convey details of flow in the aneurysm that could not be appreciated without complete review and "mental reconstruction" of the 84 acquired velocity component images.

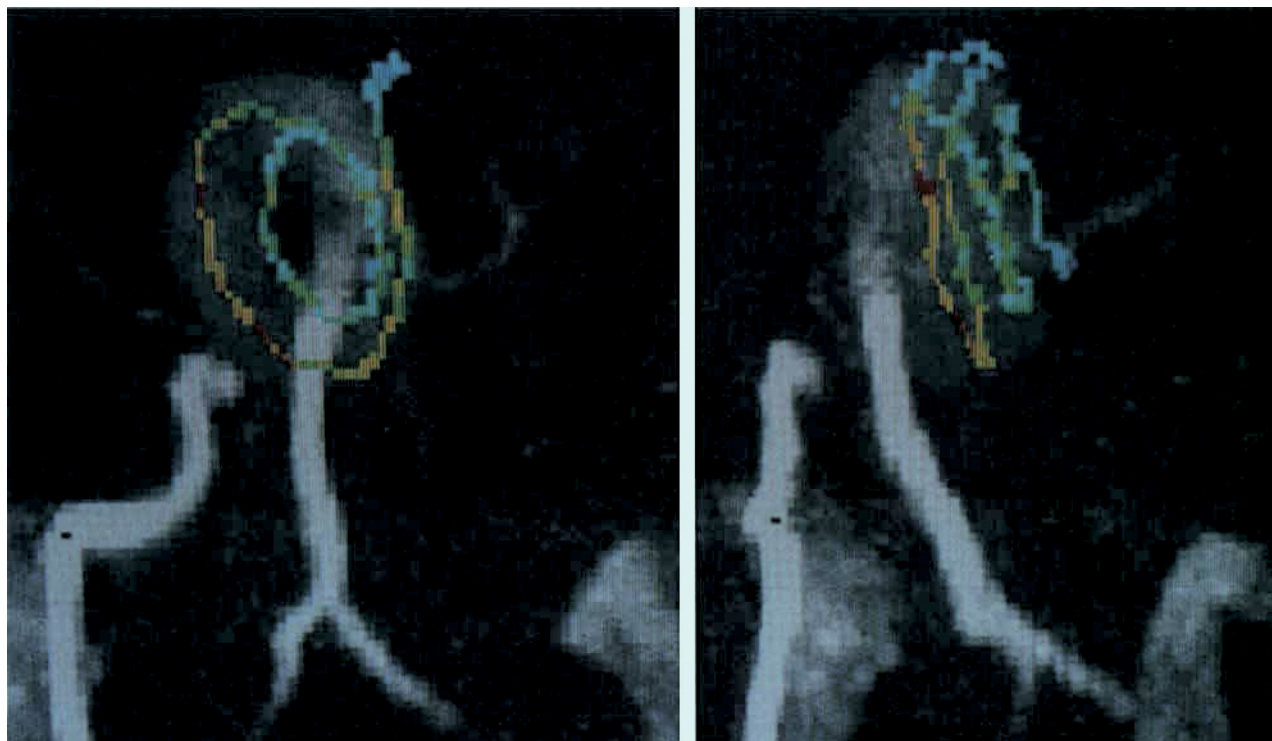
• DISCUSSION

Simulated streamlines are a valuable technique for visualizing complex 3D flow. Two-dimensional renderings of 3D phenomena, however, such as shown in the present study, do not fully illustrate the power of this method. Two commonly used techniques for adding 3D cues, such as object rotation (cine loops of projections at a number of angles) or stereo pairs, convey the 3D information in the streamlines in a far more efficient way than can be done in a single still image.

The simulation tracks each streamline for a specified time. At the end of this time, it saves a 3D volume that contains the simulated streamlines for the specified time, merged with the speed volume, and this resulting volume can be displayed as described above. However, if it is desired to display streamline evolution in time, it is possible to divide the total simulation time into a number of time intervals. In this way, intermediate results can be displayed and rendered separately or in sequence. Display of time-interval volumes can be easily combined with cine-loop rotation to show streamline evolution in time along with 3D cues. Using this technique on the results from tracking of multiple, densely packed seed particles is a powerful way to convey vessel filling-time relationships without use of a contrast agent bolus.

At present, 3D PC MR imaging has temporal resolution on the order of several minutes, and gating methods that work well with 2D PC MR imaging (8,21) are impractical. Therefore, the time-varying nature of the velocity field, caused by cardiac pulsations, is not resolved, and the velocities measured with 3D PC MR imaging are average velocities (22). Simulated streamlines computed from these data will depict trajectories through this average velocity field. However, the simulated streamline technique can use temporally resolved data when practical gating and/or rapid acquisition techniques become available. Note, however, that the ability of the computer to efficiently handle large amounts of data will become important. For example, three components of velocity for a $256 \times 256 \times 60$ -voxel volume at each of 16 phases of the cardiac cycle will occupy 377 Mbytes of data.

PC MR imaging measures a single net phase shift for each voxel. In voxels that contain distributions of velocities, this net phase shift may not correspond to the average velocity because of this partial-volume effect (23–25). The apparent velocity is a function of several factors, including the signal magnitudes of the tissues in the voxel. Suppose, for example, that half the spins within a voxel move with velocity \mathbf{v} and half are in static tissue, for a combined mean velocity of $|\mathbf{v}|/2 \cdot \mathbf{v}$. The moving spins have a signal magnitude $|M|e^{i\theta}$, where θ is proportional to velocity, and the static spins have a signal magnitude $|S|$. The measured velocity is proportional to the angle of the net signal magnitude, which is the sum $|S| + |M|e^{i\theta}$. Thus, the measured velocity will always be less than or equal to the velocity of the moving spins. When $|M|$ is large relative to $|S|$ (because of, for example, arterial inflow effects), the measured velocity will be close to that of the moving spins. In our example, the measured velocity will be greater than the mean velocity by as much as a factor of two. However, a more likely scenario is that blood flowing near the vessel wall moves slowly and experiences similar signal saturation effects as does the static tissue. In this case, $|S|$ is approximately equal to $|M|$, and so the measured velocity is approximately equal to the mean velocity. Even voxels that lie entirely within a vessel will experience partial-volume errors. Given fairly uniform signal intensity and a narrow distribution of velocities, the measured velocity will be close to the mean velocity within the voxel. However, in regions of complex flow or high shear, the measured velocity will be bi-



a.
Figure 9. Two color-coded (blue = 0 cm/sec, red = 25 cm/sec) maximum-intensity reprojections through the giant basilar tip aneurysm shown in Figure 1, seeded with a single seed particle. **(a)** Anteroposterior projection. **(b)** Forty-five-degree oblique projection.

ased toward that of the spins with the largest signal magnitude. These examples, which argue for small voxels, show that partial-volume effects may possibly lead to overestimation of mean velocities. This error may, in turn, contribute to streamline inaccuracy and/or may be part of the cause of leakers in curved vessel sections.

Simulated streamlines are not constrained to pass through the center of any given voxel. Thus, after each T seconds of simulation time, velocities must be determined at locations that are somewhere between acquired voxels by using interpolation. Consider a simulated streamline that passes close to a vessel wall. The interpolated velocity at such a location may be the average of velocities both inside and outside the vessel. Two effects are associated with this. First, computed velocities will be underestimated because of averaging with static structures. Second, static structures will, in general, have reduced signal magnitude and therefore greater variance, resulting in a "noisy" contribution to the average. These effects combined make it possible for streamlines to stick to or leak out of vessel boundaries. The effect can be mitigated to some extent by higher spatial resolution and higher signal-to-noise ratio, where possible.

In addition to facilitating better visualization of flow, simulated streamlines may have application in segmenting vessel anatomy from surrounding structures. Dense seed blocks may be placed within vessels of interest (such as was done in Figures 6 and 8), and the results may be used to segment the vessel and its

branches from its surroundings. For example, maximum-intensity projection reconstruction of the speed image can ignore voxels that have not been reached by streamlines, a technique similar to one using spatial connectivity (26).

• CONCLUSIONS

PC MR imaging can directly measure 3D velocity fields. Visualization of these measurements, which comprise a 3D vector function of 3D space, poses a difficult problem. Computation and display of simulated streamlines is a powerful technique for visualizing such functions. We have described the method, presented some initial results in phantoms and in vivo, and illustrated potential pitfalls. A potentially powerful application of this technique is the visualization of vessel filling relationships by displaying the trajectories of multiple, densely packed seed particles. Though we have described the method in the context of PC MR imaging, it is directly applicable to 3D velocity data obtained by any means available. ●

Acknowledgments: The authors gratefully acknowledge Norbert Pelc, PhD, for several important comments and suggestions and Donna Cronister for assistance in preparation of the manuscript.

References

1. Dumoulin CL, Souza SP, Walker MF, Wagle W. Three-dimensional phase-contrast angiography. *Magn Reson Med* 1989; 9:139-149.
2. van Dijk P. Direct cardiac NMR imaging of heart wall and

- blood flow velocity. *J Comput Assist Tomogr* 1984; 8:429-436.
3. Bryant DJ, Payne JA, Firmin DN, Longmore DB. Measurement of flow with NMR imaging using a gradient pulse and phase difference technique. *J Comput Assist Tomogr* 1984; 8:588-593.
4. Grover T, Singer JR. NMR spin-echo flow measurements. *J Appl Phys* 1971; 42:938-940.
5. Moran PR. A flow velocity zeugmatographic interlace for NMR imaging in humans. *Magn Reson Imaging* 1982; 1:197-203.
6. Feinberg DA, Crooks LE, Sheldon P, Hoenninger J, Watts J, Mitsuiaki A. Magnetic resonance imaging of velocity vector components of fluid flow. *Magn Reson Med* 1985; 2:555-566.
7. O'Donnell M. NMR blood flow imaging using multiecho, phase contrast sequences. *Med Phys* 1985; 12:59-64.
8. Nayler GI, Firmin DN, Longmore DB. Blood flow imaging by cine magnetic resonance. *J Comput Assist Tomogr* 1985; 10:715-722.
9. Spritzer CE, Pelc NJ, Lee JN, Evans AJ. Rapid MR imaging of blood flow with a phase-sensitive, limited-flip-angle, gradient recalled pulse sequence: preliminary experience. *Radiology* 1990; 176:255-262.
10. Pelc NJ, Bernstein MA, Shimakawa A, Glover GH. Encoding strategies for three-direction phase-contrast MR imaging of flow. *JMRI* 1991; 1:405-413.
11. Napel S, Frayne R, Rutt BK. Computation and display of 3-D flow streamlines from 3-D phase contrast MRI (abstr). In: Book of abstracts: Society of Magnetic Resonance in Medicine 1991. Berkeley, Calif: Society of Magnetic Resonance in Medicine, 1991; 88.
12. Simonetti OP, Wendt RE, Duerk JL. The significance of the point of expansion in interpretation of gradient moments and motion sensitivity. *JMRI* 1991; 1:569-577.
13. Kouwenhoven M, Hoffman MBM, Sprenger M. Reconsideration of acceleration effects in phase difference flow measurements (abstr). In: Book of abstracts: Society of Magnetic Resonance in Medicine 1991. Berkeley, Calif: Society of Magnetic Resonance in Medicine, 1991; 806.
14. Holdsworth DW, Rickey DW, Drangova M, Miller DJ, Fenster A. A computer controlled positive displacement pump for physiological flow simulation. *Med Biol Eng Comput* 1991; 29:565-570.
15. Frayne R, Gowman LM, Holdsworth DW, et al. A novel flow simulator for MR flow experiments (abstr). In: Book of abstracts: Society of Magnetic Resonance in Medicine 1990. Berkeley, Calif: Society of Magnetic Resonance in Medicine, 1990; 474.
16. Tanishita K, Suzuki J, Ohishi N, Naruse T. Fluid flow in a strongly curved pipe. *Front Med Biol Eng* 1990; 2:187-191.
17. Gowman LM, Rickey DW, Holdsworth DW, et al. Construction of a geometrically accurate vascular phantom for in vitro MRI flow studies (abstr). In: Book of abstracts: Society of Magnetic Resonance in Medicine 1990. Berkeley, Calif: Society of Magnetic Resonance in Medicine, 1990; 473.
18. Bharadvaj BK, Mabon RF, Giddens DP. Steady flow in a model of the human carotid bifurcation. I. Flow visualization. *J Biomech* 1982; 15:349-362.
19. Perktold K, Resch M. Numerical flow studies in human carotid artery bifurcations: basic discussion of the geometric factor in atherogenesis. *J Biomed Eng* 1990; 12:111-123.
20. Dumoulin CL, Hart HR. Magnetic resonance angiography. *Radiology* 1986; 161:717-720.
21. Enzmann DR, Ross MR, Marks MP, Pelc NJ. Blood flow in major cerebral arteries as measured by phase-contrast cine MR (abstr). In: Book of abstracts: Society of Magnetic Resonance in Medicine 1991. Berkeley, Calif: Society of Magnetic Resonance in Medicine, 1991; 92.
22. Rutt BK, Lee D, Vellet D, Frayne R, Napel S. Quantitative comparison of velocity measurements in the extracranial carotid arteries by 2D and 3D phase-contrast MRI versus color-flow Doppler ultrasound (abstr). In: Book of abstracts: Society of Magnetic Resonance in Medicine 1991. Berkeley, Calif: Society of Magnetic Resonance in Medicine, 1991; 91.
23. Tarnawski M, Porter DA, Graves MJ, Taylor MG, Smith MA. Flow determination in small diameter vessels by magnetic resonance imaging (abstr). In: Book of abstracts: Society of Magnetic Resonance in Medicine 1989. Berkeley, Calif: Society of Magnetic Resonance in Medicine, 1989; 896.
24. Wolf RL, Ehman RL. Determinants of accuracy and precision in MR flow volumetry (abstr). In: Book of abstracts: Society of Magnetic Resonance in Medicine 1991. Berkeley, Calif: Society of Magnetic Resonance in Medicine, 1991; 1157.
25. Pelc NJ, Sommer FG, Enzmann DR, Pelc LR, Glover GH. Accuracy and precision of phase-contrast MR flow measurements (abstr). *Radiology* 1991; 181(P):189.
26. Cline HE, Dumoulin CL, Hart HR Jr, Lorensen WE, Ludke S. 3D reconstruction of the brain from magnetic resonance images using a connectivity algorithm. *Magn Reson Imaging* 1987; 5:345-352.